

Article

One Simple Strategy towards Nitrogen and Oxygen Codoped Carbon Nanotube for Efficient Electrocatalytic Oxygen Reduction and Evolution

Jing Sun ¹, Shujin Wang ¹, Yinghua Wang ¹, Haibo Li ¹, Huawei Zhou ¹, Baoli Chen ¹, Xianxi Zhang ¹, Hongyan Chen ², Konggang Qu ^{1,*}  and Jinsheng Zhao ^{1,*} 

- ¹ School of Chemistry and Chemical Engineering, Shandong Provincial Key Laboratory/Collaborative Innovation Center of Chemical Energy Storage & Novel Cell Technology, Liaocheng University, Liaocheng 252059, China; sunjing201809@gmail.com (J.S.); wsj9898521@gmail.com (S.W.); wyh18463588761@163.com (Y.W.); lihaibo@lcu.edu.cn (H.L.); zhouhuawei@lcu.edu.cn (H.Z.); chenbaoli@lcu.edu.cn (B.C.); xxzhang3@126.com (X.Z.)
- ² Collaborative Innovation Center of Antibody Drugs, Institute of BioPharmaceutical Research, Liaocheng University, Liaocheng 252059, China; chenhongyan1123@163.com
- * Correspondence: kgqu1985@gmail.com (K.Q.); j.s.zhao@163.com (J.Z.); Tel.: +86-635-853-9077 (K.Q.); +86-635-853-9607 (J.Z.)

Received: 31 December 2018; Accepted: 2 February 2019; Published: 6 February 2019



Abstract: The development of advanced electrocatalysts for oxygen reduction and evolution is of paramount significance to fuel cells, water splitting, and metal-air batteries. Heteroatom-doped carbon materials have exhibited great promise because of their excellent electrical conductivity, abundance, and superior durability. Rationally optimizing active sites of doped carbons can remarkably enhance their electrocatalytic performance. In this study, nitrogen and oxygen codoped carbon nanotubes were readily synthesized from the pyrolysis of polydopamine-carbon nanotube hybrids. Different electron microscopes, Raman spectra and X-ray photoelectron spectroscopy (XPS) were employed to survey the morphological and componential properties. The newly-obtained catalyst features high-quality nitrogen and oxygen species, favourable porous structures and excellent electric conductivity, and thus exhibits remarkably bifunctional oxygen electrode activity. This research further helps to advance the knowledge of polydopamine and its potential applications as efficient electrocatalysts to replace noble metals.

Keywords: N, O-codoping; polydopamine; oxygen reduction; oxygen evolution; electrocatalysts; bifunctional

1. Introduction

Green and sustainable energy sources play a crucial role in addressing concerns about the global energy dilemma, pollution, and climate change [1–3]. Regenerative energy techniques involving fuel cells, metal–air batteries, and electrocatalytic hydrogen production have attracted significant interest as energy storage and conversion devices [4,5], which usually involve cathodic oxygen reduction reaction (ORR) and anodic oxygen evolution reaction (OER). Both ORR and OER contain complicated multi-electron transfer processes, which would result in sluggish reaction kinetics and consequently compromise the whole performance of the above energy devices. Electrocatalysts can drastically promote reaction rates and lower overpotentials. These features make electrocatalysts indispensable components of energy devices [6,7]. The noble metal-based materials including Pt and Ru are the most efficient electrocatalysts for ORR or OER, but their prohibitive cost and scarcity greatly impedes the proliferation of related energy technologies. In comparison, carbon materials possess a

series of satisfactory features, including natural abundance, superior electrical conductivity, tailorable structures and components, and strong anticorrosion abilities, and thus have been intensively studied as electrocatalysts during the last decade [5,8,9].

Nonmetallic heteroatom doping has been regarded as a valid strategy to increase the electrocatalytic activity of carbon materials and even achieve a particular activity towards certain electrocatalytic reactions [10]. Therefore, a rationally componential optimization is of paramount importance to develop the desired electrocatalysts. N-doping can render adjacent C atoms positive-charged, due to the greater electronegativity of N, and can also maintain the intrinsic electronic structure on account of the presence of a lone pair of nitrogen electrons. Thus, N-doping has been the most widely used [10]. Moreover, different N species significantly affect the catalytic activity of N-doping carbons. For example, Ruoff et al. found that pyridinic N (p-N) mainly determines the ORR activity of N-carbon catalysts, while graphitic N (g-N) lowers the onset potential of ORR [11]. Dai et al. suggested that g-N is responsible for ORR activity and considered p-N as active sites for the OER [12]. Most recently, oxygen species were found to be able to remarkably improve the bifunctional ORR and OER performance of carbon materials. Zhu et al. revealed that epoxy and ketene oxygen moieties provide more active sites for ORR and OER [13], whereas Wang et al. considered -COOH groups as highly bifunctionally active sites [14,15]. Although the underlying mechanisms remain controversial, N- and O-doping indeed apparently boost the bifunctional performance of carbon materials in ORR and OER. Meanwhile, dual-doped carbons have exhibited remarkably better performance than their single-doped counterparts due to the synergistic coupling effect of compatible dopants [16,17]. Significantly, N-doping within a certain range can increase the electrical conductivity of carbons [18], while the introduction of an O species is detrimental to the inherent electron configuration of sp^2 -carbons. Therefore, the effective integration of N and O dopants into the carbon matrix requires a delicate design to achieve optimal synergistic performance.

Recently, we have exploited polydopamine (PDA) as an excellent platform for doped carbons due to its unrivaled structural and componential virtues [17,19]. Robust adhesion can make PDA easily grow onto the surfaces of different solids and thus realize structural regulation [5,20]. Simultaneously, the flexible componential tunability by the post-modification of PDA facilitates the importation of multiple kinds of heteroatoms to the derived carbons [17]. The inherent N component of PDA has been utilized for the development of single N-doped and codoped carbons, with secondary dopants including B, P and S [17]. Notably, besides one nitrogen-containing group, each monomer of PDA also contains two intrinsic oxygenated groups, which can be readily available to construct the N, O-codoped carbons, but thus far, less attention has been paid to them. However, the large amount of oxygen species will certainly compromise the electrical conductivity of the resultant carbons. Carbon nanotubes (CNTs) have been widely recognized as a good electronic conductor, which can be introduced as a conductive substrate to assure a favorable electronic transfer of the integrated materials [21].

Herein, we propose a novel and simple approach to obtain N, O-codoping carbon nanotubes. PDA was first easily grafted onto the surface of multi-walled CNTs and then subjected to high-temperature carbonization. Compared to previous post-doping routes, this facile strategy can directly generate in situ and uniform N, O-codoping into the resultant carbon materials together with favorable componential and structural features. Specifically, the obtained N, O-codoped CNT (N, O-CNT) contains 2.3% nitrogen and up to 12.6% oxygen. Impressively, the inherent pyrrolic N of PDA can be completely converted into p-N and g-N, and the C=O and -COOH species dominate among different oxygen groups. All of those components are electrocatalytically active for ORR and OER. Additionally, the network structure formed by cross-stacked carbon nanotubes provide excellent electrical conductivity and smooth mass transportation. Accordingly, the newly developed N, O-CNT exhibits bifunctional activities for both ORR and OER with enhanced activity and excellent stability. Because of the robust adhesion of PDA, this facile and straightforward N, O-codoping method is significantly promising for the future energy conversion and storage applications.

2. Results

2.1. The Structural and Componential Characterization of the Catalysts

The morphologies and nanostructures of the newly-obtained N, O-CNT were firstly investigated by a scanning electron microscope (SEM) and transmission electron microscopy (TEM). As shown in Figure 1A and Figure S1, SEM images show cross-stacked CNT networks. However, as presented in the TEM images (Figure 1C), all these CNTs preserve the isolated single-tube structure. The magnified TEM images (Figure 1C and Figure S2) further manifest a layer of continuous carbon thin-film with ~2 nm-thick coating outside the lattice fringe of the CNTs, which can be ascribed to the carbonization of the uniform PDA wrapping. Notably, the kind of stacked networks formed by isolated CNTs can easily deposit onto the electrode surface with abundant intrinsic inner cavities and large pores between the CNTs, which are believed to be conducive to facile electrolyte and gas transport during the electrocatalytic processes. As shown in Figure 1D, the elemental mapping images of N, O-CNT suggest a homogeneous distribution of C, O, and N components, further indicating PDA evenly wrapped onto the surface of the CNTs. The defects and structural evolution of the CNT samples can be reflected through the intensity ratio of the D band to the G band (I_D/I_G) in the Raman spectra. As displayed in Figure 1E, the p-CNT has a small I_D/I_G ratio of 0.38, displaying an intact, pristine structure. After acid oxidation of p-CNT, ox-CNT shows a much higher I_D/I_G ratio of 1.05 arising from the oxygenated-group-enriched CNT surface. Finally, N, O-CNT can inherit a large amount of nitrogen and oxygen dopants from PDA, possibly resulting in its relatively high I_D/I_G ratio of 0.87, even after high-temperature pyrolysis. Nitrogen adsorption of N, O-CNT shows a large surface area of up to $165 \text{ m}^2 \text{ g}^{-1}$. The existence of different mesopores and macropores can be verified by the pore size distribution curve (Figure 1F), which also agrees with the electron microscopic results. Specifically, the smaller mesopores with a size of around 3–10 nm correspond to the intrinsic hollow structures of nanotubes, while the larger pores with sizes of around 10–150 nm are credited to the voids of the cross-stacking CNT networks.

FTIR measurements were used to confirm the formation of CNT-PDA hybrids (Figure 2A). The p-CNT has no characteristic peak because of its pristine structure. The peaks of ox-CNT at around 1050 and 1732 cm^{-1} indicated the presence of C–O and C=O moieties. The indole or indoline structure of PDA in CNT-PDA hybrids was certified by the coexistence of characteristic peaks at 1501 and 1609 cm^{-1} , indicating the successful wrapping of PDA onto the surface of CNT [22]. The chemical status of different components can be clearly determined by the XPS technique (Figure 2B–D and Figure S3). The presence of C, N (2.3 at.%) and O (12.6 at.%) was first confirmed by an XPS survey scan of N, O-CNT, in which the high concentration of N and O dopants also accounts for the high I_D/I_G ratio of N, O-CNT. Additionally, the deconvoluted spectra of N 1s consists of two peaks at 398.4 and 400.8 eV (Figure 2C), belonging to p-N (0.9 at.%), and g-N (1.4 at.%), while the catalytically inert pyrrolic N was not detected. The well-resolved O 1s peaks mainly comprise three peaks. More specifically, the peak at 532.5 eV is consistent with the hydroxyl (C–OH) and carbonyl (C=O) functional groups, which have a content of 5.6%. The peak at 531.3 eV is attributed to the carboxyl group (COO–) in carboxylate and the oxygen double bond to carbon, accounting for 1.7 at.%, and the peak at 533.9 eV corresponds to the oxygen single bond in esters and carboxylic acids (O=C–O), reaching 5.3% (Figure 2D). Significantly, compared with the oxygen content in p-CNT (2.3 at.%) and ox-CNT (9.5 at.%), shown in Figure S3, Figure S4 and Figure S5 [23], the relatively large number of oxygen moieties in N, O-CNT not only plays a critical role as active sites of electrocatalytic reactions [24–26], but also improves the wettability capability of the surface of resultant carbons and facilitates the electrocatalytic processes [27].

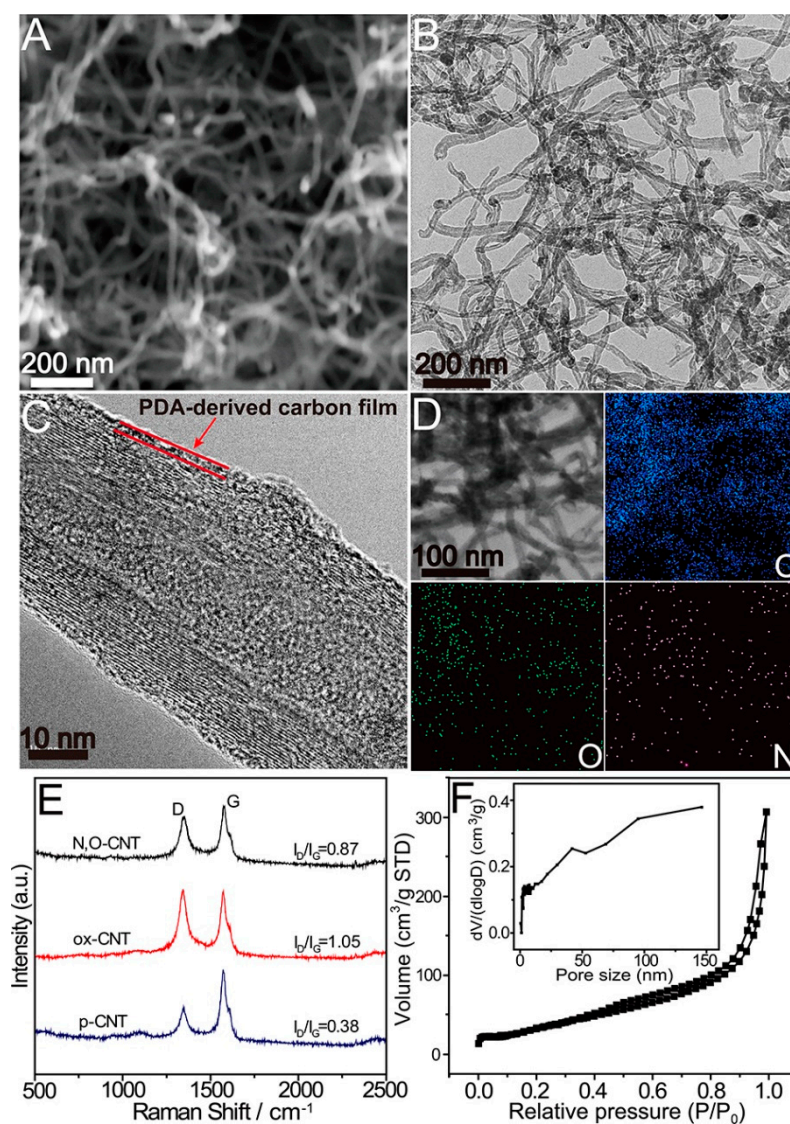


Figure 1. (A) SEM, (B) TEM and (C) the magnified TEM images of the N, O-carbon nanotube (CNT); PDA, polydopamine. (D) TEM elemental mapping of C, O, and N in N, O-CNT. (E) Raman spectra of p-CNT, ox-CNT and N, O-CNT. (F) The corresponding nitrogen adsorption–desorption isotherm of N, O-CNT, and the inset shows the pore size distribution curve.

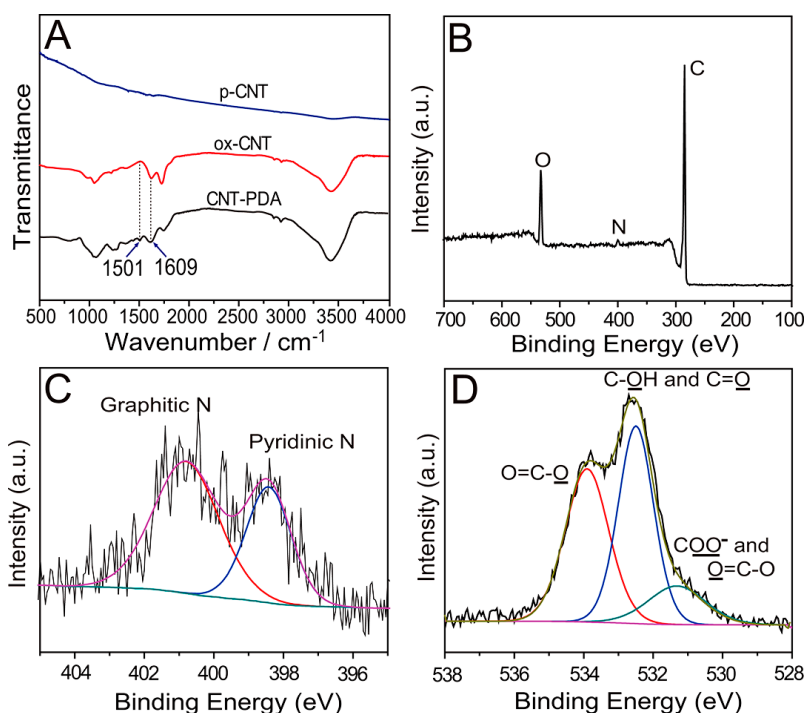


Figure 2. (A) FTIR spectra of p-CNT, ox-CNT and CNT-PDA. (B–D) XPS survey scan and the deconvoluted high-resolution spectra of N 1s and O 1s in N, O-CNT.

2.2. ORR Performance

The electrocatalytic activity for ORR was systematically evaluated on the newly-developed carbons. Firstly, the cyclic voltammograms (CVs) were examined in an O₂-saturated 0.1 M KOH electrolyte. Figure 3A displays N, O-CNT having a typical cathodic peak located at -0.28 V, and the peak potential is obviously much more positive than that of ox-CNT (-0.34 V) and p-CNT (-0.38 V). Meanwhile, the according peak current density of N, O-CNT is 3.3 mA cm⁻², much larger than that of ox-CNT (-0.94 mA cm⁻²) and p-CNT (-1.54 mA cm⁻²), both of which indicate the best ORR activity on N, O-CNT. Linear sweep voltammograms (LSVs) were then collected with a rotating disk electrode (RDE) under 1600rpm. The onset potential (η) was defined as the potential value to achieve a current density of -0.5 mA cm⁻². The η value of N, O-CNT is around -0.16 V, as shown in Figure 3B—much better than that of ox-CNT (-0.23 V) and p-CNT (-0.25 V). Of particular note, at -0.6 V, a current density up to -6.6 mA cm⁻² can be observed on N, O-CNT, which is significantly larger than the values of ox-CNT (-2.4 mA cm⁻²), p-CNT (-2.6 mA cm⁻²), and even Pt/C (-4.6 mA cm⁻²), suggesting superior electrocatalytic performance of N, O-CNT for ORR. Furthermore, N, O-CNT has no current plateau akin to that of Pt/C, caused by the limited mass transport, partly because the high surface area and hierarchically porous structures endow the N, O-CNT with abundantly available active sites and expedite diffusion ability in ORR electrocatalytic processes. The ORR catalytic kinetics of different catalysts were then assessed through Tafel slopes extracted from the LSV curves. Figure 3C illustrates a Tafel slope of 80 mV dec⁻¹ on N, O-CNT, which is much smaller than that of p-CNT (98 mV dec⁻¹) and ox-CNT (124 mV dec⁻¹); nearly approaching the value of Pt/C (74 mV dec⁻¹), the small Tafel slope of N, O-CNT manifests the enhanced ORR kinetics of N, O-CNT. To gain more insight into the electrocatalytic ability of N, O-CNT, LSVs at different rotation speeds were recorded (Figure 3D and Figure S6). The respective Koutecky-Levich (KL) plots under various potentials were linearly fitted and the kinetic limiting current density (J_k) was obtained (Figure 3E). As presented in Figure 3F, N, O-CNT has relatively high and stable J_k values under the applied potential (-0.4 to -0.8 V) compared to those of ox-CNT and p-CNT, indicating a more efficient and smooth catalytic process for ORR on N, O-CNT due to its structural advantages, as noted previously.

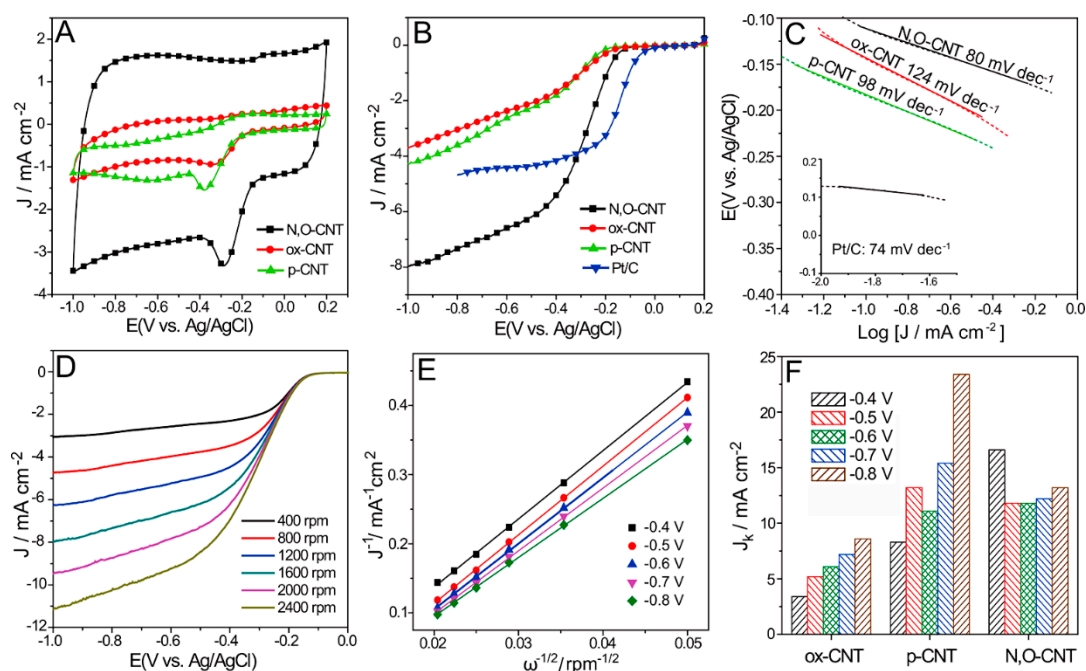


Figure 3. (A) CV curves of p-CNT, ox-CNT, and N, O-CNT in O_2 -saturated 0.1 M KOH solution. (B) LSVs at a sweep rate of 5 mV s^{-1} , and (C) Tafel slope obtained from the LSVs of p-CNT, ox-CNT, N, O-CNT, and Pt/C. (D) Linear sweep voltammograms (LSVs) of N, O-CNT at different rotating speeds from 400 to 2400 rpm. (E) K-L plots of N, O-CNT obtained at different potentials. (F) Kinetic limiting current density (J_k) of different catalysts at a potential range from -0.4 to -0.8 V.

Rotating ring disk electrode (RRDE) experiments were further conducted to quantitatively analyze the intermediate peroxide and investigate the ORR pathways on different catalysts [28]. As presented in Figure 4A,B, N, O-CNT yields 17–34% HO_2^- with a potential from -0.4 to -1.0 V, and its number of electron transfer (n) ranges from 3.3 to 3.7. In comparison, p-CNT produces ~ 41 –5% HO_2^- under identical conditions, with n ranging from 2.5 to 3.2. The n of ox-CNT was estimated from 2.3 to 3.1, with the production of ~ 44 –84% HO_2^- . These results suggest a more efficient electrocatalytic ORR process on N, O-CNT with a $4e^-$ dominated pathway. It is noteworthy that peroxide species produced in the low potential region can be continuously reduced at a high potential and contribute to the high reduction current density of N, O-CNT displayed in Figure 3B.

The long-term durability of N, O-CNT was assessed against commercial Pt/C. The test was conducted with chronoamperometry in 0.1 M KOH saturated with O_2 . As displayed in Figure 4C, Pt/C exhibits up to a 40% loss from its initial current, while N, O-CNT retains 96.7% of the original current over 20 h with a neglectable attenuation, clearly manifesting the exceedingly good stability of carbon active sites in alkaline ORR. Furthermore, the effect of methanol crossover was investigated on both N, O-CNT and Pt/C (Figure 4D). After introducing methanol into the electrolyte, the original ORR current of N, O-CNT could persist almost unaffected, confirming its robust resistance to methanol crossover. Contrarily, when 3 M methanol was added, a quick response was detected on Pt/C with the initially cathodic current directly changing to an anodic current. Consequently, the obtained N, O-CNT showed prominent durability and high selectivity to ORR, and is highly suitable as a potential candidate to replace Pt/C.

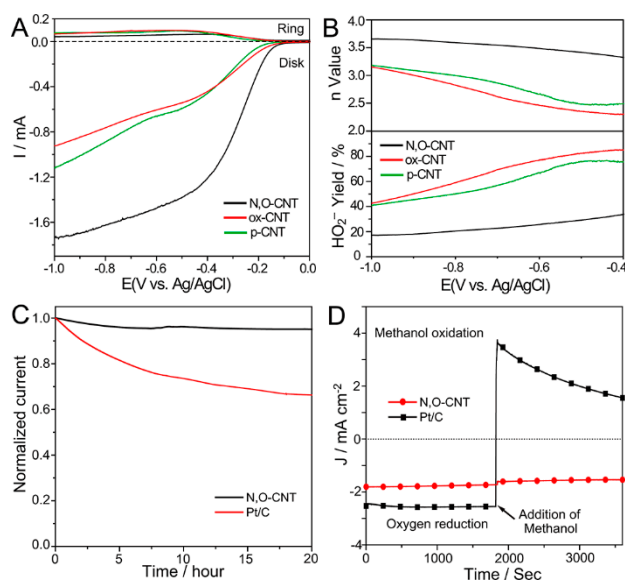


Figure 4. (A) Rotating ring disk electrode (RRDE) voltammetric response in the O_2 -saturated 0.1 M KOH at a scan rate of 5 mV s^{-1} and (B) HO_2^- yields and the corresponding electron transfer number of p-CNT, ox-CNT and N, O-CNT. (C) oxygen reduction reaction (ORR) current–time chronoamperometric response of N, O-CNT and Pt/C in O_2 -saturated 0.1 M KOH solution. (D) current–time chronoamperometric response of N, O-CNT and Pt/C before and after addition of 3 M methanol.

2.3. OER Performance

The OER catalytic performance of the obtained samples was further characterized in detail. LSVs were first performed in 0.1 M KOH, and the applied potential when generating a current density of 10 mA cm^{-2} ($E_{j=10}$) was a metric used for the comparison of different catalysts (Figure 5A). The $E_{j=10}$ for N, O-CNT is 0.65 V, which is much lower than those obtained for other samples, such as p-CNT (0.73 V) and ox-CNT (0.82 V), close to the value of IrO_2 -CNT (0.61 V). Compared to previously reported catalysts, the E_j of N, O-CNT (0.65 V) is lower than that of the various carbons, including N, O-doped carbon hydrogels [21] and N-doped carbon nanocables [29], and comparable to those of metal-containing electrocatalysts, such as $Mn_3O_4/CoSe_2$ hybrids [30], Co_3O_4/N -graphene [31], and Mn_xO_y/N -doped carbon [32]. Tafel plots were also used to evaluate the catalytic kinetics for OER (Figure 5B). N, O-CNT has a Tafel slope of 74 mV dec^{-1} , which is lowest among all the samples including p-CNT (93 mV dec^{-1}), ox-CNT (147 mV dec^{-1}), and even IrO_2 -CNT (82 mV dec^{-1}). Compared with previously reported OER catalysts, the Tafel slope of N, O-CNT is much lower than those of N, O-doped carbon hydrogels (141 mV dec^{-1}) [21], C_3N_4 /carbon nanotube composites (83 mV dec^{-1}) [33], and similar to some metal oxide OER catalysts, including Co_3O_4 /carbon nanowires (70 mV dec^{-1}) [34], CoO/N -graphene (71 mV dec^{-1}) [35], and Co_3O_4/N -graphene (67 mV dec^{-1}) [31], implying its enormously beneficial catalytic kinetics for OER. The catalytic kinetics of different samples can be further evidenced by the electrochemical impedance spectrum (EIS). As illustrated in Figure 5C, N, O-CNT has a much smaller impedance compared to that of p-CNT and ox-CNT, confirming its greatly unimpeded reaction kinetics. An electrochemical durability test of N, O-CNT for OER was then carried out. As illustrated in the inset of Figure 4D, a long-time potential cycling conducted on N, O-CNT signified insignificant reduction of the catalytic performance after 1000 cycles (Figure 5D). The LSV curves show that 91.2% of the initial current density remained after 1000 potential cycles, confirming the remarkable electrochemical stability of the N, O-CNT for OER.

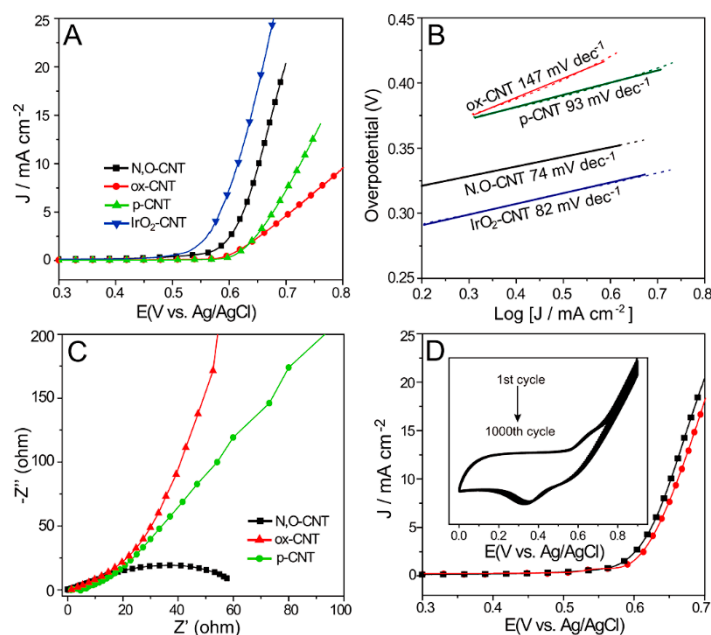


Figure 5. (A) Oxygen evolution reaction (OER) LSVs at a sweep rate of 5 mVs^{-1} and (B) OER Tafel plots of p-CNT, ox-CNT, N, O-CNT, and IrO_2 -CNT. (C) The electrochemical impedance spectra (recorded at 0.65 V) of p-CNT, ox-CNT, and N, O-CNT. (D) Electrochemical durability test of N, O-CNT for OER, the LSV plots before and after 1000 cycles, and inset are the CV plots at 50 mV s^{-1} for 1000 cycles. (A) The overall LSV curve of N, S-CN in the potential range of -0.8 to 0.8 V , ΔE ($E_{j=10} - E_{j=-3}$) is a metric for bifunctional ORR and OER activity (Inset: The value of ΔE for various catalysts reported previously).

To better investigate the overall oxygen electrode activity, the different metrics for OER and ORR on various catalysts were all compared and displayed in Figure 6A and Table S1, including onset potential, Tafel slope, the potential at -3 mA cm^{-2} for ORR ($E_{j=-3}$), and $E_{j=10}$ for OER [36]. The difference in potential between $E_{j=10}$ and $E_{j=-3}$ was designated as ΔE , i.e., $\Delta E = E_{j=10} - E_{j=-3}$. The smaller ΔE means better overall oxygen electrode activity. Notably, N, O-CNT displays a ΔE of 0.92 V , much smaller than that of p-CNT (1.40 V) and ox-CNT (1.61 V), which is also superior compared to the previously reported non-metallic materials (e.g., N-graphene/CNT [37], $\Delta E = 0.96 \text{ V}$; C_3N_4 -CNT, $\Delta E = 1.30 \text{ V}$) [36], noble-metals (e.g., Pt/C, $\Delta E = 1.16 \text{ V}$; Ru/C, $\Delta E = 1.01 \text{ V}$; Ir/C, $\Delta E = 0.92 \text{ V}$) [38], and transition-metals (e.g., NiCo_2S_4 @N/S-rGO [39], $\Delta E = 0.98 \text{ V}$; NiCo_2O_4 /G [40], $\Delta E = 1.13 \text{ V}$) [32,38], and close to that of phosphorus-doped carbon nitride/carbon-fiber paper (PCN-CFP, 0.91 V) [36], N, S-CN (0.88 V) [6], and Co/N-C-800 (0.86 V) [41]. Figure 6B summarizes a detailed comparison of different bifunctional oxygen electrocatalysts, demonstrating the excellent catalytic performance of N, O-CNT towards a bifunctional ORR and OER.

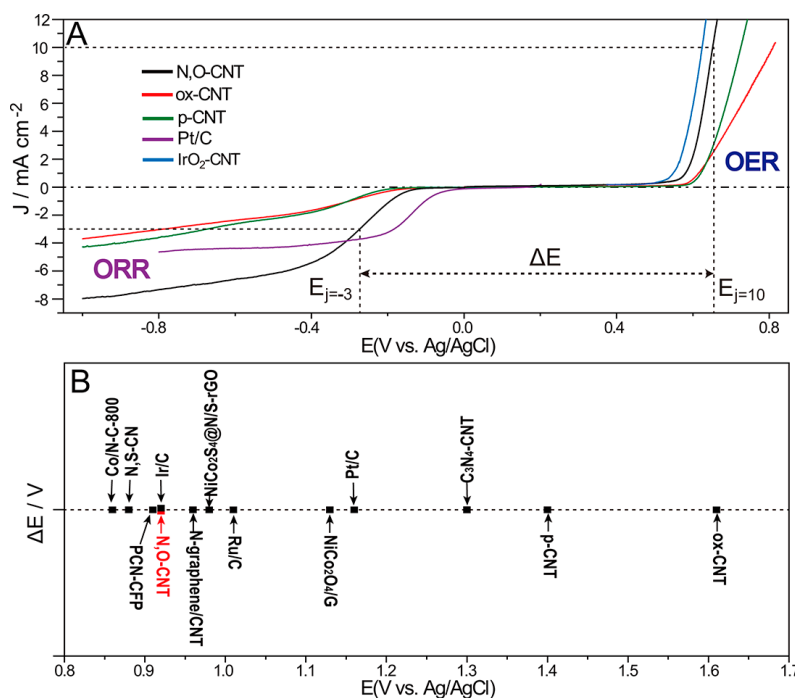


Figure 6. (A) The overall LSV curve of N, O-CNT in the potential range of -1.0 to 0.8 V, (B) the value of ΔE of N, O-CNT and the comparison with various catalysts reported previously.

The efficiently bifunctional performance of the N, O-CNT catalyst for ORR and OER could arise from the following three aspects: First, N, O-CNT contains 2.3% N and 12.6% O, and thus produces a large population of active sites. The N element has a larger electronegativity and can afford a positive charge density to the adjacent C atoms, which are generally considered electrocatalytically active centers [33,42]. Furthermore, N, O-CNT only consists of favored p-N and g-N, while no pyrrolic N was found, which reportedly has little catalytic effect [11]. Meanwhile, different oxygen groups, including the C=O and COOH moieties, have been found to facilitate OER and ORR due to the electron withdrawing effect and enhanced adsorption of reaction intermediates [14,15,43]. A host of oxygen groups up to 12.6% in N, O-CNT would, therefore, greatly promote the bifunctional activity of obtained carbons. Secondly, a large surface area of catalysts can enhance the exposure of active sites and assure their sufficient utilization. The porous structure of N, O-CNT, shown by nitrogen adsorption, can also be assessed by electrochemical double-layer capacitance (C_{dl}). Figure 7 displays the C_{dl} of N, O-CNT as 4.4 mF cm^{-2} , while the values of p-CNT and ox-CNT are 1.4 and 2.5 mF cm^{-2} . As C_{dl} reflects the electrocatalytic active surface area, the bigger C_{dl} of N, O-CNT illustrates the larger active surface of N, O-CNT, which can promote its apparent ORR and OER performance. Moreover, the different porous structures of N, O-CNT can guarantee an unblocked channel for benign mass transfer [22]. Thirdly, the employed CNT substrate can provide excellent electronic conductivity, which has been confirmed by the EIS study. Additionally, PDA-derived defective carbons can be firmly incorporated with CNTs because of the robustly adhesive PDA, which ensures an unimpeded charge transfer and the long-term stability of the integrated carbons. All these manifold virtues come together to make the developed N, O-CNT an advanced bifunctional ORR and OER electrocatalyst.

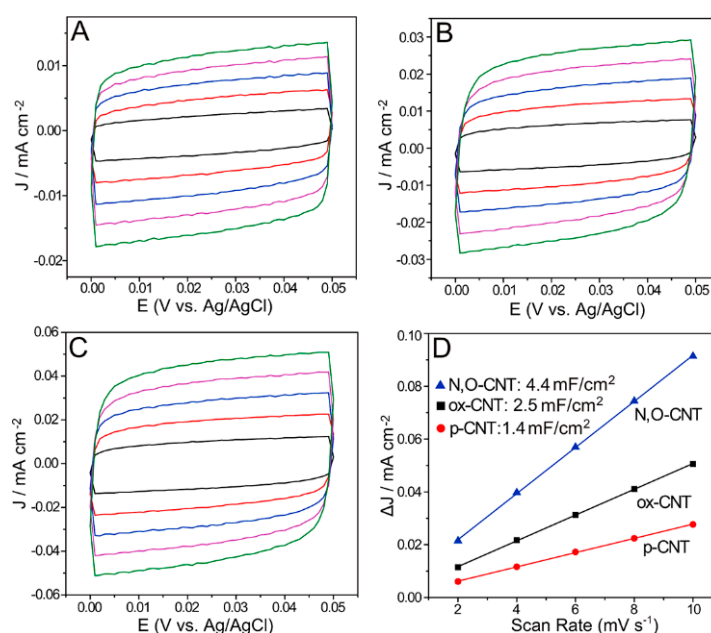


Figure 7. CV curves at different scan rates (2, 4, 6, 8, and 10 mV s^{-1}) of (A) p-CNT, (B) ox-CNT, and (C) N, O-CNT. (D) The corresponding difference in the current density at 0.025 V plotted against scan rate; the calculated C_{dl} values are shown as the inset.

3. Materials and Methods

3.1. Preparation of N, O-CNT

The ox-CNT was synthesized first. The purchased primitive CNTs were ultrasonicated in a mixed solution of sulfuric acid (98%) and nitric acid (70%) with 3:1 *v/v* for 10 h and washed repeatedly with copious water. The obtained sample was incubated with 5 M HCl at 50 °C for 24 h to eliminate metal impurities. After lyophilization, ox-CNT was sonicated in water to obtain 1 mg mL^{-1} dispersion.

To prepare N, O-CNT, 100 mg of dopamine (DA) was added into 100 mL of the above ox-CNT dispersion followed by 100 mL of phosphate buffered saline (PBS, 0.4 M, pH = 8.5) added. Under a magnetic stirring, the reaction in the mixed solutions was kept for 24 h. The CNT-PDA samples were obtained by centrifugation and washing with water. The N, O-CNT was synthesized by the pyrolysis of CNT-PDA in a tube furnace under a N_2 atmosphere. The pyrolysis temperature was first set at 400 °C for 2 h with a heating rate of 1 °C min^{-1} , then at 800 °C for 3 h with a heating rate of 5 °C min^{-1} .

3.2. Electrochemical Characterization

The electrochemical measurements were conducted on an electrochemical workstation (CHI 760C, CH Instruments, Austin, TX, USA). The inks of different catalysts were prepared as follows: The catalysts of 2 mg were dispersed under ultrasonication into 1 ml water to make a well-distributed suspension. Then, 20 μL of catalyst ink was dropped on the electrode surface. 5 μL of 0.5 wt.% Nafion aqueous solution was pipetted on the electrode and air dried. The three-electrode cell system was employed in a standard five-neck electrolyzer and consisted of an RDE glassy carbon working electrode, a Ag/AgCl reference electrode in saturated AgCl-KCl solution, and a platinum wire as counter electrode. Cyclic voltammogram (CV) and linear sweep voltammogram (LSV) tests were performed with a scan rate of 50 and 5 mV s^{-1} , respectively. The RRDE measurement was conducted to evaluate the catalytic efficiency of samples for ORR, and its detailed experiments are presented in the Supplementary Materials.

The EIS tests of the OER were conducted under an AC voltage with 5 mV amplitude in a frequency range from 100,000 to 1 Hz and recorded at 0.65 V vs. Ag/AgCl. The C_{dl} of the as-synthesized materials was obtained from double-layer charging curves using CVs in a potential range of 0–0.05 V. The capacitive currents, i.e., $\Delta J_{|j_a-j_c|}$ @ 0.025 V, were plotted as a function of the CV scan rate. The linear relationship was observed with a slope two-times larger than the C_{dl} value.

4. Conclusions

In conclusion, by virtue of PDA, a new and simple strategy, with attractive componential and structural features, was presented to prepare N, O-CNT. The resultant codoped carbon is characterized by highly efficient N and O components, favorable pore architecture, and high surface areas, and hence exhibits a remarkably bifunctional performance for ORR and OER with outstanding activity and excellent stability. Due to the versatile features of PDA, this work could offer a novel insight into rationally developing PDA-derived doped carbons, which are greatly promising as substitutes for noble metals in relevant energy conversion fields.

Supplementary Materials: The following are available online at <http://www.mdpi.com/2073-4344/9/2/159/s1>, Figure S1: SEM image of N, O-CNT, Figure S2: The magnified TEM images of the N, O-CNT, Figure S3: XPS high-resolution spectra of C1s of N, O-CNT, Figures S4 and S5: XPS survey scans and the deconvoluted high-resolution spectra of p-CNT and ox-CNT. Figure S6: LSVs at different rotating speeds from 0 to 2400 rpm and the K-L plots obtained at different potentials, Table S1: Comparison of the different OER and ORR metrics of the obtained catalysts.

Author Contributions: Conceptualization, K.Q.; Methodology, J.S. and S.W.; Formal analysis, Y.W. and H.L.; Data curation, H.Z. and B.C.; Writing—original draft preparation, J.S. and H.C.; Writing—review and editing, K.Q. and J.Z.; Supervision, X.Z. and K.Q.; Project administration, K.Q.

Acknowledgments: This work was financially supported by the National Natural Science Foundation of China (21601078, 21503104), Natural Science Foundation of Shandong Province (ZR2016BQ21, ZR2014BQ010, ZR2016BQ20), Colleges and Universities in Shandong Province Science and Technology Projects (J16LC03, J16LC05, J17KA097), and the Doctoral Program of Liaocheng University (318051608).

Conflicts of Interest: The authors declare no conflict of interest.

References

1. Dresselhaus, M.S.; Thomas, I.L. Alternative energy technologies. *Nature* **2001**, *414*, 332–337. [[CrossRef](#)] [[PubMed](#)]
2. Norskov, J.K.; Christensen, C.H. Toward Efficient Hydrogen Production at Surfaces. *Science* **2006**, *312*, 1322–1323. [[CrossRef](#)] [[PubMed](#)]
3. Chu, S.; Cui, Y.; Liu, N. The path towards sustainable energy. *Nat. Mater.* **2017**, *16*, 16–22. [[CrossRef](#)] [[PubMed](#)]
4. Steele, B.C.H.; Heinzel, A. Materials for fuel-cell technologies. *Nature* **2001**, *414*, 345. [[CrossRef](#)] [[PubMed](#)]
5. Zhang, Q.; Luo, F.; Ling, Y.; Guo, L.; Qu, K.; Hu, H.; Yang, Z.; Cai, W.; Cheng, H. Constructing Successive Active Sites for Metal-free Electrocatalyst with Boosted Electrocatalytic Activities Toward Hydrogen Evolution and Oxygen Reduction Reactions. *ChemCatChem* **2018**, *10*, 5194–5200. [[CrossRef](#)]
6. Qu, K.; Zheng, Y.; Dai, S.; Qiao, S.Z. Graphene oxide-polydopamine derived N, S-codoped carbon nanosheets as superior bifunctional electrocatalysts for oxygen reduction and evolution. *Nano Energy* **2016**, *19*, 373–381. [[CrossRef](#)]
7. Zhang, J.; Zhao, Z.; Xia, Z.; Dai, L. A metal-free bifunctional electrocatalyst for oxygen reduction and oxygen evolution reactions. *Nat Nano* **2015**, *10*, 444–452. [[CrossRef](#)]
8. Chu, Y.; Gu, L.; Ju, X.; Du, H.; Zhao, J.; Qu, K. Carbon Supported Multi-Branch Nitrogen-Containing Polymers as Oxygen Reduction Catalysts. *Catalysts* **2018**, *8*, 245. [[CrossRef](#)]
9. Zheng, Y.; Jiao, Y.; Qiao, S.Z. Engineering of Carbon-Based Electrocatalysts for Emerging Energy Conversion: From Fundamentality to Functionality. *Adv. Mater.* **2015**, *27*, 5372–5378. [[CrossRef](#)]
10. Jin, H.; Guo, C.; Liu, X.; Liu, J.; Vasileff, A.; Jiao, Y.; Zheng, Y.; Qiao, S.-Z. Emerging Two-Dimensional Nanomaterials for Electrocatalysis. *Chem. Rev.* **2018**, *118*, 6337–6408. [[CrossRef](#)]

11. Lai, L.; Potts, J.R.; Zhan, D.; Wang, L.; Poh, C.K.; Tang, C.; Gong, H.; Shen, Z.; Lin, J.; Ruoff, R.S. Exploration of the active center structure of nitrogen-doped graphene-based catalysts for oxygen reduction reaction. *Energy Environ. Sci.* **2012**, *5*, 7936–7942. [[CrossRef](#)]
12. Yang, H.B.; Miao, J.; Hung, S.-F.; Chen, J.; Tao, H.B.; Wang, X.; Zhang, L.; Chen, R.; Gao, J.; Chen, H.M.; et al. Identification of catalytic sites for oxygen reduction and oxygen evolution in N-doped graphene materials: Development of highly efficient metal-free bifunctional electrocatalyst. *Sci. Adv.* **2016**, *2*, e1501122. [[CrossRef](#)] [[PubMed](#)]
13. Lv, J.-J.; Li, Y.; Wu, S.; Fang, H.; Li, L.-L.; Song, R.-B.; Ma, J.; Zhu, J.-J. Oxygen Species on Nitrogen-Doped Carbon Nanosheets as Efficient Active Sites for Multiple Electrocatalysis. *ACS Appl. Mater. Interfaces* **2018**, *10*, 11678–11688. [[CrossRef](#)] [[PubMed](#)]
14. Liu, Z.; Zhao, Z.; Wang, Y.; Dou, S.; Yan, D.; Liu, D.; Xia, Z.; Wang, S. In Situ Exfoliated, Edge-Rich, Oxygen-Functionalized Graphene from Carbon Fibers for Oxygen Electrocatalysis. *Adv. Mater.* **2017**, *29*, 1606207. [[CrossRef](#)] [[PubMed](#)]
15. Kordek, K.; Jiang, L.; Fan, K.; Zhu, Z.; Xu, L.; Al-Mamun, M.; Dou, Y.; Chen, S.; Liu, P.; Yin, H.; et al. Two-Step Activated Carbon Cloth with Oxygen-Rich Functional Groups as a High-Performance Additive-Free Air Electrode for Flexible Zinc–Air Batteries. *Adv. Energy Mater.* **2018**, *2018*, 1802936. [[CrossRef](#)]
16. Liang, J.; Jiao, Y.; Jaroniec, M.; Qiao, S.Z. Sulfur and Nitrogen Dual-Doped Mesoporous Graphene Electrocatalyst for Oxygen Reduction with Synergistically Enhanced Performance. *Angew. Chem. Int. Ed.* **2012**, *51*, 11496–11500. [[CrossRef](#)] [[PubMed](#)]
17. Qu, K.; Zheng, Y.; Zhang, X.; Davey, K.; Dai, S.; Qiao, S.Z. Promotion of Electrocatalytic Hydrogen Evolution Reaction on Nitrogen-Doped Carbon Nanosheets with Secondary Heteroatoms. *ACS Nano* **2017**, *11*, 7293–7300. [[CrossRef](#)] [[PubMed](#)]
18. Ismagilov, Z.R.; Shalagina, A.E.; Podyacheva, O.Y.; Ischenko, A.V.; Kibis, L.S.; Boronin, A.I.; Chesalov, Y.A.; Kochubey, D.I.; Romanenko, A.I.; Anikeeva, O.B.; et al. Structure and electrical conductivity of nitrogen-doped carbon nanofibers. *Carbon* **2009**, *47*, 1922–1929. [[CrossRef](#)]
19. Qu, K.; Zheng, Y.; Jiao, Y.; Zhang, X.; Dai, S.; Qiao, S.Z. Polydopamine-Inspired, Dual Heteroatom-Doped Carbon Nanotubes for Highly Efficient Overall Water Splitting. *Adv. Energy Mater.* **2017**, *7*, 1602068. [[CrossRef](#)]
20. Qu, K.; Wang, Y.; Zhang, X.; Chen, H.; Li, H.; Chen, B.; Zhou, H.; Li, D.; Zheng, Y.; Dai, S. Polydopamine-Derived, In Situ N-Doped 3D Mesoporous Carbons for Highly Efficient Oxygen Reduction. *ChemNanoMat* **2018**, *4*, 417–422. [[CrossRef](#)]
21. Chen, S.; Duan, J.; Jaroniec, M.; Qiao, S.-Z. Nitrogen and Oxygen Dual-Doped Carbon Hydrogel Film as a Substrate-Free Electrode for Highly Efficient Oxygen Evolution Reaction. *Adv. Mater.* **2014**, *26*, 2925–2930. [[CrossRef](#)] [[PubMed](#)]
22. Qu, K.; Zheng, Y.; Dai, S.; Qiao, S.Z. Polydopamine-graphene oxide derived mesoporous carbon nanosheets for enhanced oxygen reduction. *Nanoscale* **2015**, *7*, 12598–12605. [[CrossRef](#)] [[PubMed](#)]
23. Datsyuk, V.; Kalyva, M.; Papagelis, K.; Parthenios, J.; Tasis, D.; Siokou, A.; Kallitsis, I.; Galiotis, C. Chemical oxidation of multiwalled carbon nanotubes. *Carbon* **2008**, *46*, 833–840. [[CrossRef](#)]
24. Jiang, Y.; Yang, L.; Sun, T.; Zhao, J.; Lyu, Z.; Zhuo, O.; Wang, X.; Wu, Q.; Ma, J.; Hu, Z. Significant contribution of intrinsic carbon defects to oxygen reduction activity. *ACS Catal.* **2015**, *5*, 6707–6712. [[CrossRef](#)]
25. Ishizaki, T.; Chiba, S.; Kaneko, Y.; Panomsuwan, G. Electrocatalytic activity for the oxygen reduction reaction of oxygen-containing nanocarbon synthesized by solution plasma. *J. Mater. Chem. A* **2014**, *2*, 10589–10598. [[CrossRef](#)]
26. Lu, Z.; Chen, G.; Siahrostami, S.; Chen, Z.; Liu, K.; Xie, J.; Liao, L.; Wu, T.; Lin, D.; Liu, Y. High-efficiency oxygen reduction to hydrogen peroxide catalysed by oxidized carbon materials. *Nat. Catal.* **2018**, *1*, 156. [[CrossRef](#)]
27. Zhang, R.; Jing, X.; Chu, Y.; Wang, L.; Kang, W.; Wei, D.; Li, H.; Xiong, S. Nitrogen/oxygen co-doped monolithic carbon electrodes derived from melamine foam for high-performance supercapacitors. *J. Mater. Chem. A* **2018**, *6*, 17730–17739. [[CrossRef](#)]
28. Zhou, R.; Zheng, Y.; Jaroniec, M.; Qiao, S.-Z. Determination of the Electron Transfer Number for the Oxygen Reduction Reaction: From Theory to Experiment. *ACS Catal.* **2016**, *6*, 4720–4728. [[CrossRef](#)]

29. Tian, G.-L.; Zhang, Q.; Zhang, B.; Jin, Y.-G.; Huang, J.-Q.; Su, D.S.; Wei, F. Toward Full Exposure of “Active Sites”: Nanocarbon Electrocatalyst with Surface Enriched Nitrogen for Superior Oxygen Reduction and Evolution Reactivity. *Adv. Funct. Mater.* **2014**, *24*, 5956–5961. [[CrossRef](#)]
30. Gao, M.-R.; Xu, Y.-F.; Jiang, J.; Zheng, Y.-R.; Yu, S.-H. Water Oxidation Electrocatalyzed by an Efficient Mn₃O₄/CoSe₂ Nanocomposite. *J. Am. Chem. Soc.* **2012**, *134*, 2930–2933. [[CrossRef](#)]
31. Liang, Y.; Li, Y.; Wang, H.; Zhou, J.; Wang, J.; Regier, T.; Dai, H. Co₃O₄ nanocrystals on graphene as a synergistic catalyst for oxygen reduction reaction. *Nat. Mater.* **2011**, *10*, 780–786. [[CrossRef](#)] [[PubMed](#)]
32. Masa, J.; Xia, W.; Sinev, I.; Zhao, A.; Sun, Z.; Grütze, S.; Weide, P.; Muhler, M.; Schuhmann, W. MnxOy/NC and CoxOy/NC Nanoparticles Embedded in a Nitrogen-Doped Carbon Matrix for High-Performance Bifunctional Oxygen Electrodes. *Angew. Chem. Int. Ed.* **2014**, *53*, 8508–8512. [[CrossRef](#)] [[PubMed](#)]
33. Ma, T.Y.; Dai, S.; Jaroniec, M.; Qiao, S.Z. Graphitic Carbon Nitride Nanosheet–Carbon Nanotube Three-Dimensional Porous Composites as High-Performance Oxygen Evolution Electrocatalysts. *Angew. Chem. Int. Ed.* **2014**, *53*, 7281–7285. [[CrossRef](#)] [[PubMed](#)]
34. Ma, T.Y.; Dai, S.; Jaroniec, M.; Qiao, S.Z. Metal–Organic Framework Derived Hybrid Co₃O₄-Carbon Porous Nanowire Arrays as Reversible Oxygen Evolution Electrodes. *J. Am. Chem. Soc.* **2014**, *136*, 13925–13931. [[CrossRef](#)] [[PubMed](#)]
35. Mao, S.; Wen, Z.; Huang, T.; Hou, Y.; Chen, J. High-performance bi-functional electrocatalysts of 3D crumpled graphene-cobalt oxide nanohybrids for oxygen reduction and evolution reactions. *Energy Environ. Sci.* **2014**, *7*, 609–616. [[CrossRef](#)]
36. Ma, T.Y.; Ran, J.; Dai, S.; Jaroniec, M.; Qiao, S.Z. Phosphorus-Doped Graphitic Carbon Nitrides Grown In Situ on Carbon-Fiber Paper: Flexible and Reversible Oxygen Electrodes. *Angew. Chem. Int. Ed.* **2015**, *54*, 4646–4650. [[CrossRef](#)] [[PubMed](#)]
37. Tian, G.-L.; Zhao, M.-Q.; Yu, D.; Kong, X.-Y.; Huang, J.-Q.; Zhang, Q.; Wei, F. Nitrogen-Doped Graphene/Carbon Nanotube Hybrids: In Situ Formation on Bifunctional Catalysts and Their Superior Electrocatalytic Activity for Oxygen Evolution/Reduction Reaction. *Small* **2014**, *10*, 2251–2259. [[CrossRef](#)]
38. Gorlin, Y.; Jaramillo, T.F. A Bifunctional Nonprecious Metal Catalyst for Oxygen Reduction and Water Oxidation. *J. Am. Chem. Soc.* **2010**, *132*, 13612–13614. [[CrossRef](#)]
39. Liu, Q.; Jin, J.; Zhang, J. NiCo₂S₄@graphene as a Bifunctional Electrocatalyst for Oxygen Reduction and Evolution Reactions. *ACS Appl. Mater. Interfaces* **2013**, *5*, 5002–5008. [[CrossRef](#)]
40. Lee, D.U.; Kim, B.J.; Chen, Z. One-pot synthesis of a mesoporous NiCo₂O₄ nanoplatelet and graphene hybrid and its oxygen reduction and evolution activities as an efficient bi-functional electrocatalyst. *J. Mater. Chem. A* **2013**, *1*, 4754–4762. [[CrossRef](#)]
41. Su, Y.; Zhu, Y.; Jiang, H.; Shen, J.; Yang, X.; Zou, W.; Chen, J.; Li, C. Cobalt nanoparticles embedded in N-doped carbon as an efficient bifunctional electrocatalyst for oxygen reduction and evolution reactions. *Nanoscale* **2014**, *6*, 15080–15089. [[CrossRef](#)] [[PubMed](#)]
42. Zheng, Y.; Jiao, Y.; Chen, J.; Liu, J.; Liang, J.; Du, A.; Zhang, W.; Zhu, Z.; Smith, S.C.; Jaroniec, M.; et al. Nanoporous Graphitic-C₃N₄@Carbon Metal-Free Electrocatalysts for Highly Efficient Oxygen Reduction. *J. Am. Chem. Soc.* **2011**, *133*, 20116–20119. [[CrossRef](#)] [[PubMed](#)]
43. Li, L.; Yang, H.; Miao, J.; Zhang, L.; Wang, H.-Y.; Zeng, Z.; Huang, W.; Dong, X.; Liu, B. Unraveling Oxygen Evolution Reaction on Carbon-Based Electrocatalysts: Effect of Oxygen Doping on Adsorption of Oxygenated Intermediates. *ACS Energy Lett.* **2017**, *2*, 294–300. [[CrossRef](#)]

